



HAL
open science

Experiments on tuned UHBR open-test case fan ECL5/CATANA : stability limit

Anne Lise Fiquet, Alexandra P. Schneider, Benoît Paoletti, Xavier Ottavy,
Christoph Brandstetter

► **To cite this version:**

Anne Lise Fiquet, Alexandra P. Schneider, Benoît Paoletti, Xavier Ottavy, Christoph Brandstetter. Experiments on tuned UHBR open-test case fan ECL5/CATANA : stability limit. Journal of Engineering for Gas Turbines and Power, 2023, pp.1-12. 10.1115/1.4063717 . hal-04066078v2

HAL Id: hal-04066078

<https://hal.science/hal-04066078v2>

Submitted on 27 Nov 2023

HAL is a multi-disciplinary open access archive for the deposit and dissemination of scientific research documents, whether they are published or not. The documents may come from teaching and research institutions in France or abroad, or from public or private research centers.

L'archive ouverte pluridisciplinaire **HAL**, est destinée au dépôt et à la diffusion de documents scientifiques de niveau recherche, publiés ou non, émanant des établissements d'enseignement et de recherche français ou étrangers, des laboratoires publics ou privés.

Experiments on tuned UHBR open-test-case fan ECL5/CATANA: Stability limit

Anne-Lise Fiquet, Alexandra P. Schneider, Benoit Paoletti, Xavier Ottavy and Christoph Brandstetter

Univ. Lyon, École Centrale de Lyon,
CNRS, Univ. Claude Bernard Lyon 1,
INSA Lyon, LMFA, UMR5509,
69130, Écully, France

Research of the past decades has shown that the operating range of modern fans and compressors is often limited by aeroelastic phenomena before the onset of pure aerodynamic instability. Prediction of these mechanisms is challenging for state-of-the-art numerical methods, particularly for configurations with flexible wide-chord blades. To provide a benchmark configuration for the community, the composite-material fan stage ECL5, representative of near future Ultra-High-Bypass Ratio architectures has been designed at Ecole Centrale de Lyon and recently shared as an open-test-case. In research program CATANA, different configurations with variable tuning and intake geometries are investigated experimentally, and here we present a comprehensive aeroelastic study of the tuned reference configuration. The study encompasses the investigation of the whole subsonic and transonic operating range using multi-physical instrumentation.

A characterization of structural properties under running conditions is analyzed in comparison to individual blade measurements and FEM-predictions. The stability limit is investigated at different speedlines. At transonic conditions, rotating stall occurred without aeroelastic precursors. Severe non-synchronous-vibrations were observed at subsonic speeds and limited the operating range before the onset of rotating stall. Through a detailed analysis of the aeroelastic coupling mechanism, a full characterization of interacting modes is presented. The challenging prediction of this coupled phenomenon and the discrepancy to aeroelastic simulations are discussed. The results are a promising benchmark for future method development, particularly involving high-fidelity methods.

NOMENCLATURE

EO Engine Order
FEM Finite Element Method
FSI Fluid-Structure Interaction

LE Leading Edge
LES Large Eddy Simulation
LCO Limit Cycle of Oscillations
LRANS Linearized RANS
MC Mid-Chord
NSV Non-Synchronous Vibration
OGV Outlet Guide Vane
RANS Reynolds-Averaged Navier-Stokes
TE Trailing Edge
TT Tip-timing
TCS Turbulence Control Screen
UHBR Ultra-High-Bypass-Ratio
URANS Unsteady RANS
 N_v Nodal diameter [-]
 N_a Aerodynamic wave number [-]
 P_s Static pressure [bar]
 P_t Total pressure [bar]
 T_t Total temperature [K]
 c_{ax} Axial chord [-]
 f Frequency [Hz]
 dx Axial displacement [mm]
 dr Radial displacement [mm]
 P_{atmo} Atmospheric pressure [bar]
 ε Strain [$\mu m/m$]
 ε_{M_j} Scope limit of Mode-j [$\mu m/m$]
 Π_t Total pressure ratio [-]
 \dot{m}_{std} Standard mass-flow rate [kg/s]
 $rd\theta$ Tangential displacement [mm]
 ω Angular frequency [rad/s]
 Ω Angular velocity [rad/s]
 ΔP_s Non-synchronous pressure fluctuation [bar]
• S Stationary frame of reference
• R Rotating frame of reference
• a Aerodynamic disturbance
• v Structural vibration
• r Rotor
• PS Pressure side
• SS Suction side
 $\hat{\cdot}$ Fourier coefficient
 $\bar{\cdot}$ Temporal average

INTRODUCTION

The operation range of modern turbofan architectures is typically limited by instabilities arising from interaction between aerodynamic, aeroelastic and aeroacoustic phenomena. Extensive research has been conducted in the past decades, focusing on aerodynamic instabilities i.a. [1, 2, 3, 4, 5, 6, 7, 8], and countermeasures such as mistuning [9, 10]. For low-speed fans the dedicated research program CA3VIAR has put a specific focus on flutter [11]. Significant attention has been addressed to non-synchronous blade vibration (NSV) at near stall conditions, which can be safety critical. Recent studies have shown that the onset of NSV arises from the propagation of aerodynamic disturbances, travelling around the circumference and phase-locking with structural blade eigenmodes [12, 13, 14]. This aeroelastic phenomenon differs from classic aeroelastic instabilities such as flutter [15, 16], and its prediction is challenging due to multi-physical interactions which require advanced numerical methods.

Enormous knowledge gaps exist concerning these highly coupled fluid-structure instabilities, which are particularly relevant for future Ultra-High-Bypass-Ratio (UHBR) concepts [17]. The open questions concern the predictivity of state-of-the-art aeroelastic methods as best-practice methods from known high-speed geometries are not transferable to the new generation of low-speed fans. The aerodynamic design is different, with low hub-to-tip ratios and wide chord at midspan and tip. This causes complex aerodynamic fields with high swirl angles near the hub and radial flow migration, affecting the aeroelastic behaviour [18, 19, 13]. The torsionally flexible blades require significant tip clearance and cause aerodynamic blockage, which is known to favour convective disturbances. In contrast to conventional high-speed fans, the shift from transonic to subsonic occurs at higher relative rotation speeds, and hence alter aeroelastic problems. This particularly applies to the issue of NSV caused by flow separation at the sharp leading edges, which are optimized for transonic flow. Because of these issues, predictivity of established CFD methods is not evident as publications on low-speed fans have showed in recent years [13]. The main problem for method development is the lack of detailed validation data, with comprehensive information on the test setup, structural properties, real tip clearance and stagger angle. The objective of the European CleanSky-2 project CATANA¹ is to fill these gaps. A new open-test-case fan stage ECL5, representative of near-future UHBR fan concepts with carbon-fibre composite blades, has been designed by Ecole Centrale de Lyon. The geometry has been shared with the community as an open-test case [20]. Recently, the first experiments have been conducted on the test facility Phare-2 [21], with the core section presented in Fig. 1. The aerodynamic baseline results of this study are presented in the accompanying paper [22], providing detailed aerodynamic measurements, real geometry measurements and an analysis of blade-

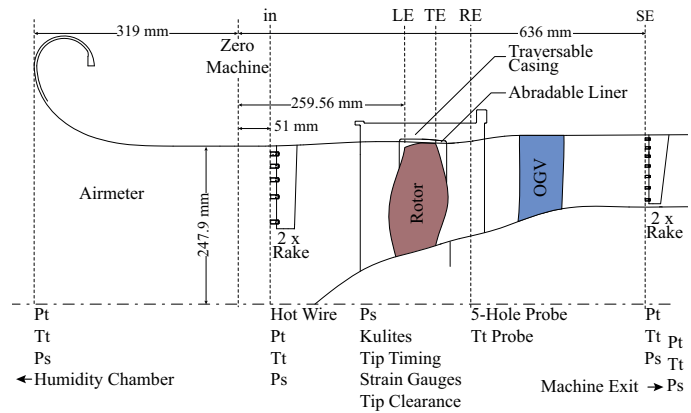


Fig. 1. Schematic view of the machine core and probe positions

to-blade variations. In this publication, a comprehensive analysis of the aeroelastic behaviour is presented, focusing on the experimentally observed phenomena close to the stability limit. Different rotational speeds and operating conditions are considered, showing the evolution of coherent aerodynamic disturbances with blade vibration, and discussed in comparison with numerical simulations, highlighting challenges for accurate prediction.

In addition, structural measurements of the individual blades are discussed in comparison to rotating measurements and FEM predictions. Complementary measurements of vibration at stabilized and transient conditions for different speedlines using strain gauges and tip timing are analyzed.

The vibration measurements are combined with techniques to measure aerodynamic disturbances which interact with blade vibrations: multi-sensor cross correlation of circumferentially distributed sensors in the rotor-section to determine convective propagation speeds and nodal diameters. The available instrumentation allows to clearly characterize the aeroelastic interaction, but also to analyze blade-to-blade variations due to unintended system asymmetry. As will be shown, general trends of already published theoretical data on the setup are proven through the experiment, but differences in critical modes, propagation speeds and non-negligible system asymmetry are observed.

Combined with the shared geometry and mechanical properties of the open-test-case, the presented results provide a benchmark dataset to validate unsteady coupled and uncoupled simulations near the stability limit. The data enables a deeper understanding of the variety of phenomena leading to instability and sheds light on non-linear effects which are relevant for future composite architectures.

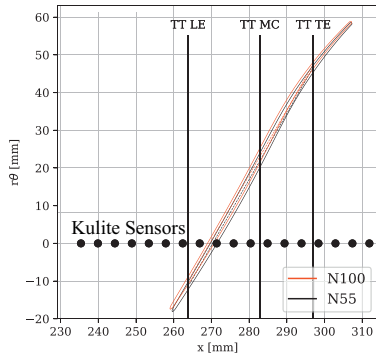
EXPERIMENTAL SETUP AND METHODS

Open Test Case Fan

The fan stage shown in Fig. 1 is composed of 16 rotor blades and 31 outlet guide vanes (OGV). The downstream OGV is constructed conventionally from aluminium vanes.

¹catana.ec-lyon.fr

a) Tip Geometry and Instrumentation (figure to scale)



b) Fan assembly and Ping-Test setup



c) Tip Timing and Strain Gauge Instrumentation

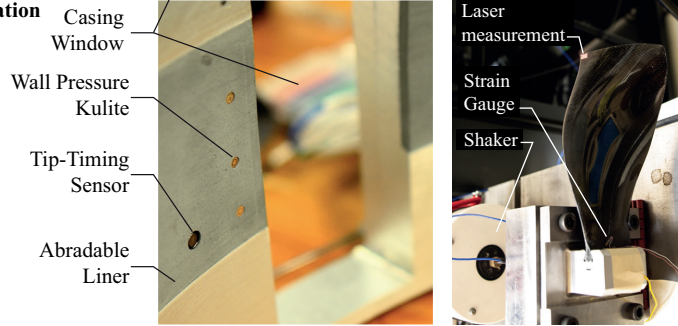
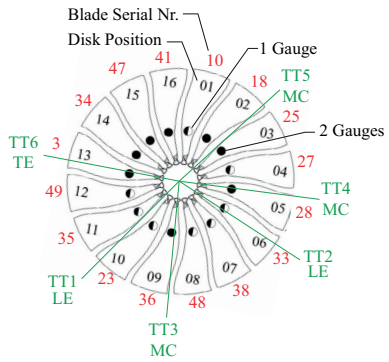


Fig. 2. Overview of unsteady measurements: (a) tip geometry and casing-mounted measurements, (b) fan assembly and ping-test setup and (c) tip-timing and strain gauge instrumentation

This figure shows the instrumentation used to derive the fan performance, with two rakes installed in the machine intake (plane *in*) and two extra rakes downstream of the OGVs (plane *SE*) equally distributed around the circumference (e.g. 180°). The design speed is 11000 rpm, requiring transonic blade design near the tip as shown in Fig. 2(a). The aerodynamic design point was numerically predicted at a standard mass-flow rate of 36.0 kg/s, the fan-stage total pressure ratio is 1.35 and the isentropic efficiency is 92%. A total of 48 blades have been manufactured from pre-impregnated carbon fibre layers, which are cut, oriented and stacked according to FEM simulations, described in reference [23]. After demolding, blades were machined at hub, tip and leading edge. Each fabricated blade was finally controlled in a 3D-scanner, frequency response determined via ping-test, weighted (static moment and mass) and selected blades were used for tomography analysis to investigate possible air-inclusions. A detailed report² on the fabricated blades is available. From the set of 48 blades, two configurations of 16 blades each have been selected for investigations: a) the reference configuration with maximum tuning of blade eigenfrequencies of the first three eigenmodes which is the subject of the present publication, and b) a mistuned configuration which will be investigated in the future.

The experiments were performed at the open cycle test facility Phare-2 at Ecole Centrale de Lyon. The ma-

chine is driven by an electrical motor with a maximum power of 3MW. Details on the facility are given in [21]. A turbulence control screen (TCS) is installed in front of the machine core to ensure homogeneous inflow conditions and reduce large scale turbulence [24]. For performance measurements the machine is instrumented with rakes [22], but for the operability measurements presented here, all intrusive instrumentation was removed. During experiments, the machine was stabilized at constant rotation speed, corrected to ISA conditions and the operation point varied through incremental closing of an axisymmetric throttle downstream of the core section. Details on the aerodynamic investigation of the stage, blade individual tip-clearance and stagger measurements are presented in [22]. Aerodynamic phenomena in the rotor section are investigated using unsteady wall pressure measurements in multiple axial and circumferential positions as shown in Fig. 2(a).

Vibration Measurement

Strain gauge The mechanical behavior of the rotor is captured using blade-mounted strain gauges, allowing to derive blade vibrations in the rotating frame of reference. Each blade is instrumented by at least one strain-gauge located at the suction side between the hub and the root. Half of the number of blades are also instrumented by a second gauge at the pressure side, detailed in Fig. 2(c). Blades are sequentially numbered as presented, also indicating the serial number of the manufactured blade at the

²Reports of Composite Aeroelastic ANd Aeroacoustics project H2020

respective disk position.

In a ping-test setup, shown in Fig. 2(b), the reference configuration has shown a maximum frequency deviation of 0.65% from the respective mean value, the mistuned configuration approximately 1.5%. This setup was used to calibrate the sensitivity of each strain gauge compared to modal deflection at the blade tip using a Laser interferometer.

Tip-timing system A tip-timing (TT) system is used to resolve tip clearance and deflection in the stationary frame of reference and (travelling) structural modes. Six calibrated capacitive sensors for tip-timing and clearance measurements are integrated in the casing wall Fig. 2. The sensors are located at three different axial positions to enable measurements of the tip deflection along the chord: near the leading-edge at $11\%c_{ax}$ (TT LE), at mid-chord at $62\%c_{ax}$ (TT MC) and near the trailing-edge at $88\%c_{ax}$. Using a one-per-revolution signal, each blade can be clearly identified in the measurements.

During a synchronous excitation, the rotor blades vibrate with a frequency which is an integer multiple of rotation speed. The amplitude is maximal at the resonance point and a phase shift of 180° occurs when passing the resonance. The synchronous analysis is based on the run time deviation relative to the undeflected blade for all possible sensor pairs. With 6 sensors, a total of 15 sensor pairs is possible. Fitting of theoretical function based on a harmonic oscillator to experimental curves for all sensor pairs enables to derive vibration amplitude, frequency, phase and damping, more details in [25]. To enable this, the characteristics of relevant vibration modes from FEM simulations are given as input to identify modes. The FEM simulations furthermore allow to scale modal deflection at the blade tip to the maximum Goodman-stress, whose location in the blade varies from mode to mode. The FEM simulations, described in [23] consider static loading and centrifugal force. For the first three eigenmodes, the critical tip deflection is presented in Fig. 4. All values shown in this publication can hence be presented relative to critical stress, the ratio defined as scope limit.

Non-synchronous vibrations occur at frequencies which are not a multiple integer of the rotational speed and arise from aerodynamic or aeroacoustic excitation. The analysis of non-synchronous vibrations considers the time-of-arrival of successive blades at certain sensor, with details on the analysis method provided by [25].

Both synchronous and non-synchronous analysis is complementary performed using the individual strain gauges, whose signals are transferred via telemetry and acquired continuously and synchronized with the unsteady wall-pressure instrumentation. The tip-timing system is independent of the unsteady instrumentation, but it has its own one-per-revolution signal.

Cross-correlation methods to determine propagation speed of aerodynamic and structural modes

In [14] a method was introduced to determine the propagation speed of aerodynamic disturbances which lock in with structural vibrations during NSV. The method is based on pairwise cross-correlations of multiple circumferentially distributed Kulite wall-pressure sensors. The cross-correlation $s_1 \star s_2$ between the signals of sensor 1 and 2 is given by Eq. 1 where I is the number of samples per revolution and j the phase-shift. The result is normalized by the respective standard deviation of each signal σ .

$$s_1 \star s_2(j) = \frac{1}{I} \frac{1}{\sigma(s_1)\sigma(s_2)} \sum_{i=0}^{I-j-1} \Delta s_1(i) \Delta s_2(i+j) \quad (1)$$

This correlation can be mapped from a phase shift j to a propagation speed normalized by the rotor speed as determined by Eq. 2 using the circumferential spacing of two sensors $\Delta\theta_{12}$.

$$\frac{\Omega}{\Omega_r} = \frac{\Delta\theta_{12}/360^\circ}{j/I} \quad (2)$$

The accuracy is increased by performing pairwise cross-correlations of all circumferentially distributed sensors leading to a common propagation speed vector. Aliased correlation peaks are removed by considering the minimum correlation for each propagation speed. In the present study, this method is applied on pressure fluctuation signals yielding the propagation speed of aerodynamic disturbances in the stationary frame of reference Ω_a^s and also for strain gauge signals on different rotor blades. The propagation speed of a vibration mode in the rotating frame of reference Ω_v^r is derived as described before and then mapped to the nodal diameter N_v with Eq. 3 for each mode with the respective eigenfrequencies $\omega_v^R = 2\pi f_v^R$.

$$N_v = \frac{\omega_v^R}{\Omega_v^r} \quad (3)$$

SYSTEM CHARACTERIZATION

The modal analysis of the rotor blade was carried out with FEM solver ANSYS using a cyclic symmetry condition and the anisotropic properties of the composite. The approach and the setup is detailed in [20]. Fig. 3 shows the predicted modal displacement from Mode-1 to Mode-3. Mode-1 is a bending mode with a low torsional component leading to a purely circumferential displacement. To reduce the risk of flutter, specific attention was paid in the design phase to minimize the torsional component. Mode-2 instead shows a pronounced torsional component at the blade tip near the leading edge, known to be critical for Non-Synchronous Blade Vibration (NSV). In contrast, Mode-3 is a torsional mode with the torsional center located at the leading edge at the tip. Fig. 4 represents the tip deflection at design speed for all modes with a scale factor of 4 compared to 100% of scope limit from FEM results. The hot shape of the tip is indicated in light grey and the axial positions of tip-timing sensors are denoted. As presented in [23], the eigenmodes and frequencies are

slightly different for a nodal diameter of $N_v = 1$. As this assembly mode was not observed in the measurements, it is omitted for brevity but was considered by the tip-timing system. The mode shapes presented here are representative of nodal diameter $N_v = 0$, and $N_v = \pm 2 \dots 8$.

Table 1. FEM predictions for design speed of eigenfrequencies; ping-test eigenfrequencies for 0% speed; maximal modal displacement and deformation at SG locations at design point (100% speed) for 100% of scope limit based on FEM results

	Mode-1	Mode-2	Mode-3
$f_{N_v=0, \text{FEM}} [\text{Hz}]$	250	605	870
$f_{N_v=0, \text{ping-test}} [\text{Hz}]$	243	596	838
$dx [\text{mm}]$	0.25	1.61	0.84
$dr [\text{mm}]$	0.22	0.49	0.12
$rd\theta [\text{mm}]$	2.26	1.28	0.68
$\epsilon_{SS} [\mu\text{m}/\text{m}]$	451.59	254.75	603.76
$\epsilon_{PS} [\mu\text{m}/\text{m}]$	356.69	226.62	686.36

Using the Goodman diagram of the used carbon-fiber composite material, the maximal stress allowed for each relevant mode is determined at design point. Modal so-

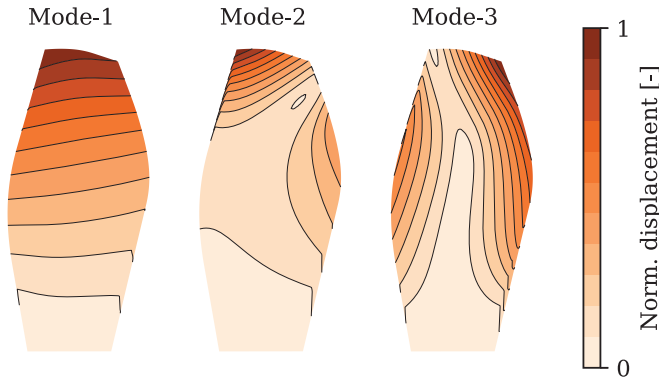


Fig. 3. FEM simulations of blade modeshapes of $N_v=0$

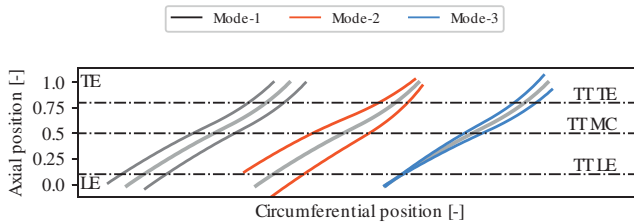


Fig. 4. Tip deflection at design speed for Mode-1, Mode-2 and Mode-3 ($N_v = 0$) and axial position of tip-timing sensors. Amplitude represents 400% scope limit at design speed

lutions (displacement, strain and stress) from FEM are thus scaled to correspond to 100% of scope limit. Table 1 summarizes the maximal tip displacement (dx , dr and $rd\theta$) and strain at the respective gauge positions (ϵ_{SS} and ϵ_{PS}) at design point for 100% of scope limit, as well as the frequencies f from FEM-prediction at 100% speed and measured in the ping-test. For all modes, the prediction exceeds the measured values, particularly for Mode-3. Blade individual measurements are presented in the appendix.

Synchronous vibrations

For synchronous mode identification, a slow acceleration from 1000rpm to 11600rpm at constant ramp of 25 rpm/s was conducted at a throttle position corresponding to peak efficiency at design speed. To increase forced response amplitudes a measurement without TCS is analyzed in the following that allows clear mode identification.

Fig. 5 shows the Campbell diagram of the fan from strain gauge signals averaged over all blades. Crossings with engine orders are highlighted with tip-timing data as black circles scaled to scope limit. The strain data are raw and not scaled to scope limit as the factor varies with frequency. The FEM prediction of blade eigenfrequencies for Mode-1, Mode-2 and Mode-3 are shown as dashed lines. A significant resonance between Mode-1 and EO2 is observed at 7680 rpm at a scope limit of 42% determined by tip-timing. The crossings Mode-1/EO3 and Mode-1/EO4 present amplitudes lower than 10% of scope limit. The dominant crossing for Mode-2 is reached at 10000rpm with EO4 leading to a scope limit of 8%. The crossing Mode-3/EO5 occurs at 10190rpm with an amplitude of 31% of scope limit. The Campbell diagram shows that the predicted frequencies are slightly higher than those of manufactured blades over the whole speed range. Stiffening of all modes with rotation speed is most prominent for Mode-2 and well predicted by FEM. All modes are predicted too stiff by FEM, with the highest difference of 4% for Mode-3. The FEM prediction of Mode-1 is very accurate with less than 1% difference to the measured crossing. The maximum modal scope limit for each blade associated to crossings Mode-1/EO2, Mode-2/EO4, Mode-3/EO5 is plotted in Fig. 6. The response is mostly symmetric, with variations of the order of 5%.

Deviation of the blade eigenfrequency relative to the average frequency for each blade is presented in Fig. 7 at dominant crossings: Mode-1/EO2, Mode-2/EO4 and Mode-3/EO5. The variation is significantly smaller than in the ping test. Also, the pattern observed in the ping test is not found in the rotating measurements. This observation will be subject of further studies, as two completely independent setups for the ping test have been realized and produced repeatable patterns. The same applies to the tip-timing measurements under rotation, which are also coherent with strain-gauge data, hence the observation is significant.

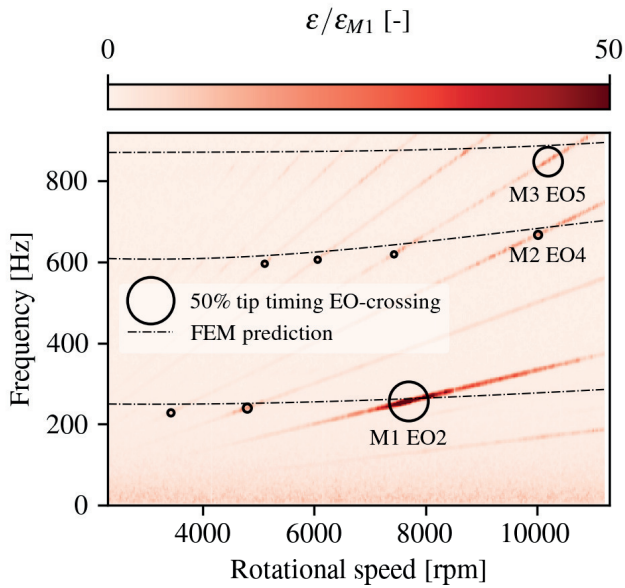


Fig. 5. Campbell diagram from averaged strain gauges signal, tip-timing data at crossings with FEM-prediction of blade eigenfrequencies for Mode-1, Mode-2 and Mode-3

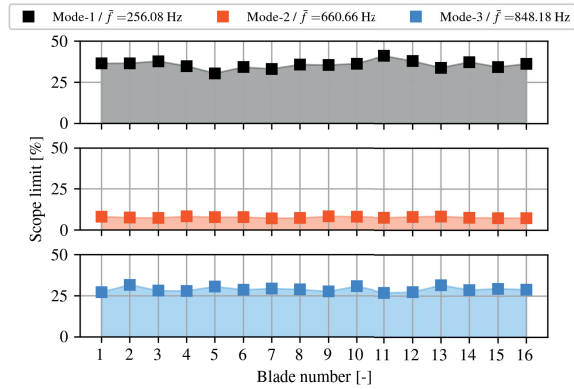


Fig. 6. Maximal modal scope limit for each blade at crossing Mode-1/EO2, Mode-2/EO4 and Mode-3/EO5 from tip-timing data

INVESTIGATION OF STABILITY LIMIT

Global observations

A systematic investigation of the stability limit was conducted at constant speedlines. The throttle was incrementally closed in steps of 0.1% of its section and the machine stabilized for at least 30 seconds. Experiments were aborted either through observation of rotating stall in online-surveillance of Kulite-sensors or if vibration amplitudes exceeded 50% of scope limit on individual blades, by opening rapidly the throttle to ensure the safety of the fan.

Fig. 8 represents a contour map of the respective scope limit value averaged over all rotor blades as a function of mass-flow and machine pressure ratio. To remove synchronous vibration, only the unsteady signal is derived by subtracting a continuous ensemble average from the data and band-pass filtering the signals for each

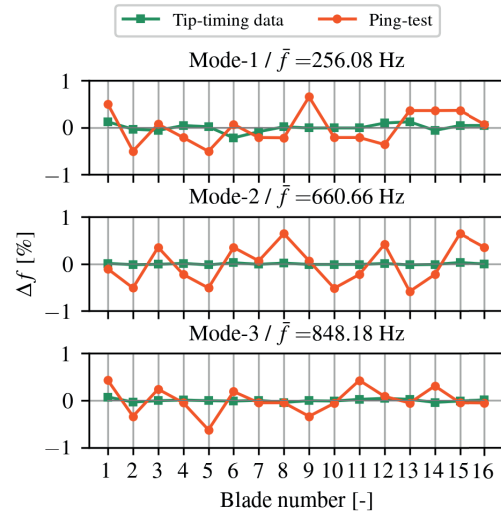


Fig. 7. Deviation of blade eigenfrequency for Mode-1, Mode-2 and Mode-3 at crossing Mode-1/EO2, Mode-2/EO4 and Mode-3/EO5 from tip-timing data and ping-test

mode [14]. The contour map represents the average peak value during each stabilized measurement. As no rakes were installed for these measurements, the pressure ratio was measured between the atmospheric pressure in the anechoic chamber and at the machine exit, 1 meter downstream of the stage [21]. Hence, the shown values are slightly lower than presented in [22], which uses rakes close to the stage. Yet, the shape of each characteristic is similar. Mass-flow rate is calculated using the same instrumentation. The individual stabilized conditions are depicted as black dots.

Between 55% speed and 90% speed all experiments have been aborted due to vibration limits reaching 50% scope limit for Mode-2 before the onset of rotating stall. Mode-1 and Mode-3 reached maximum limits of approximately 25% scope limit. At 80% and 90% speed Mode-1 responds earlier than Mode-2 with levels of approximately 10% scope limit at the respective point of peak pressure, i.e. when the total pressure characteristic rolls over. In this context Mode-3 is the less critical.

At 100% and 105% the machine entered rotating stall without any vibratory precursors but reaching critical vibration levels during stall. The speedline at 95% presents an intermediate behaviour, with moderate vibration amplitudes but sudden occurrence of rotating stall cells. At the last shown operating point the machine could be stabilized with intermittent occurrence of rotating stall.

To validate these observations, accelerations and decelerations between the individual speedlines have been conducted at the respective second to last throttle condition and did not reveal any further limitations of the operating map.

Analysis of NSV at 80% speed

Representative of a subsonic speedline, a detailed analysis of the aeroelastic behaviour at 80% relative

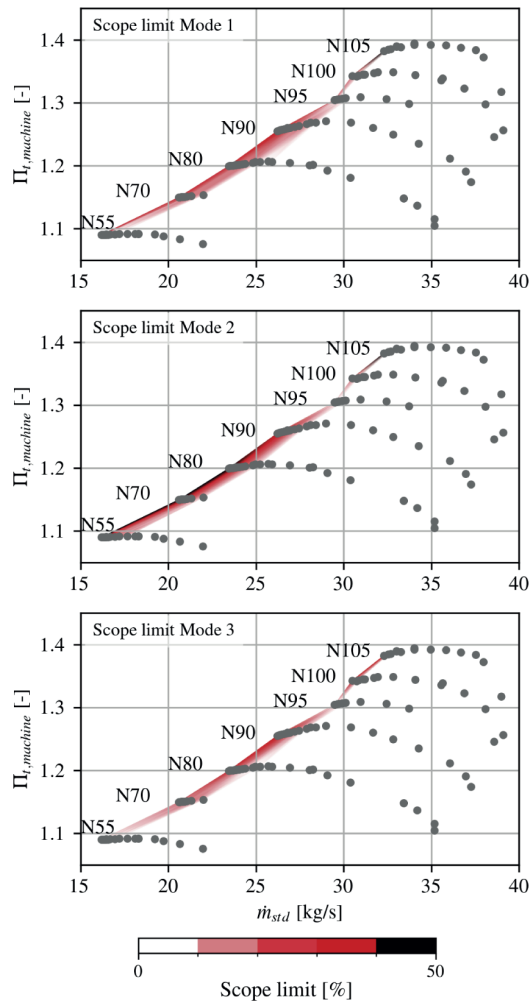


Fig. 8. Fan stage characteristics with maximal modal amplitude for Mode-1, Mode-2 and Mode-3 from strain gauge data

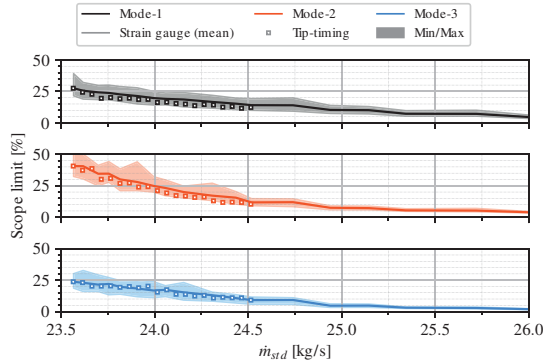


Fig. 9. Transient evolution of modal amplitude at 80% of design speed from strain gauge and tip-timing data

speed is presented in the following for the mass-flow range between peak pressure (26 kg/s) and the last stable operating point (23.6 kg/s). The evolution of non-synchronous vibration amplitudes for each mode is shown in Fig. 9, presenting a continuous evolution, which is coherent between tip-timing and the strain gauges. The average amplitude is

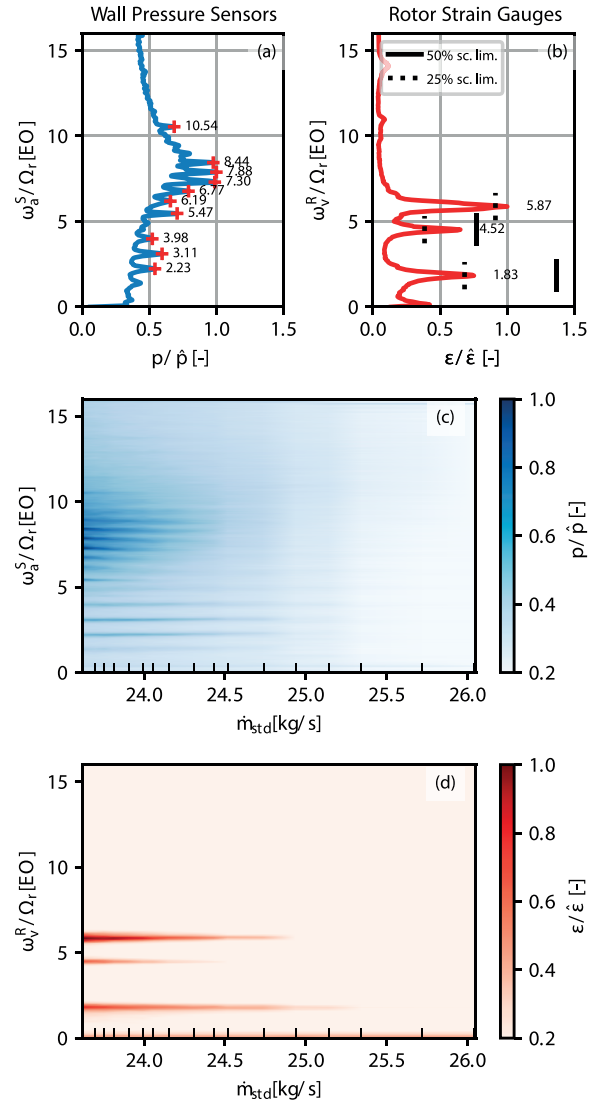


Fig. 10. Spectral analysis of casing-wall pressure near rotor leading edge (a,c) and rotor-strain gauge signals (b,d) during NSV onset at 80% speed, normalized to maximum value

represented by the continuous curve with a colored band for maximal and minimal values. No sudden increase of blade vibration is observed such as expected for classical flutter.

To investigate coherence between aerodynamic disturbances and structural vibrations, both unsteady wall pressure sensors and strain gauges are analyzed. Fig. 10 (a) presents the average spectrum of distributed Kulites in the leading edge plane for NSV condition at 80% speed and a mass-flow rate of 23.6 kg/s. Ensemble averaged signals have been subtracted to isolate non-synchronous signals. The well-known broadband disturbance discussed under the term "Rotating Instabilities" [1] is observed, centred around Engine order 8, i.e. half the blade passing frequency. Distinct peaks are denoted which will be analysed in the following section using the methods described in [26]. The contour plot in Fig. 10(c)

shows the evolution of this spectrum over mass-flow, indicating a continuous increase of unsteady amplitudes. All individual peaks are already present at higher mass-flow conditions but slightly shift in frequency. The two graphs in Fig. 10(b, c) present the same analysis for the rotor-strain gauges, averaging all blades. Clearly, the three first eigenmodes are depicted, all continuously increasing as discussed before. Comparison of (c) and (d) emphasizes the coherent rise in amplitudes of blade vibration and unsteady pressure with decreasing mass-flow.

As all vibration modes are present, it is not obvious to assign a distinct interaction mode between aerodynamic disturbances and structural nodal diameters. Using the method of pairwise cross-correlations of 8 Kulites distributed around the circumference in the leading edge, the graph presented in Fig. 11 is derived depicting the dominant propagation speed of aerodynamic disturbances. At higher mass-flow rates, a distinct peak at $\Omega_a^s/\Omega_r = 1$ is observed, indicating disturbances or non-stationary inhomogeneity travelling with the rotor. An additional peak is already present but at lower amplitude at $\Omega_a^s/\Omega_r = 0.57$. As the machine is throttled, this peak increases in intensity and becomes dominant at low mass-flow rates. The relative speed indicates a convective phenomenon, that travels backwards in the relative frame of reference.

The same analysis is performed with the rotor-strain gauges to derive structural nodal diameters. All strain gauges are band-pass filtered around the respective eigenmode, all possible pairwise cross-correlations calculated and the propagation speed mapped to derive a nodal diameter, presented in Fig. 12. The figure shows only Mode-2 and Mode-3, as no coherent values were obtained for Mode-1. Mode-2 develops a forward travelling pattern of $N_v = 7$ with reduced mass-flow, shifting to $N_v = 6$ when the measurement was aborted. Mode-3 is even clearer correlated at $N_v = 3$ and finally shifts to $N_v = 2$ at a mass-flow rate of 23.6kg/s.

With these informations, it is now possible to clearly characterize all modes observed at this speedline, and explain individual peaks in Fig. 10, summarized in Tab. 2. To highlight locking phenomena between aerodynamic and structure, the phase-locked pressure waves are in bold text.

- The dominant peak in the pressure spectrum at EO 7.88 is related to blade vibration of Mode-3 in nodal diameter $N_v = 2$. This blade eigenmode is locked-in with a backward travelling aerodynamic disturbance of wave number $N_a = -14$, propagating circumferentially at a speed of $\Omega_a^S/\Omega_r = 0.58$.
- The distinct further pressure peak at EO 10.52 corresponds to blade Mode-2 in nodal diameter $N_v = 6$, modulating with aerodynamic disturbances of wave number $N_a = -10$, travelling at $\Omega_a^S/\Omega_r = 0.54$ and producing the pressure peak at EO 5.47.
- All further pressure peaks between EO 3.98 and 8.44 correspond to non-locked-in aerodynamic disturbances of consequent wave numbers, all propagating

with a speed of approximately $\Omega_a^S/\Omega_r = 0.56$. This is coherent with observations of a different low-speed fan in [26]

- The pressure peak at EO 3.11 might interact with the blade Mode-1, $N_v = -5$ which was observed at low amplitude in tip timing, but is negligible in comparison.

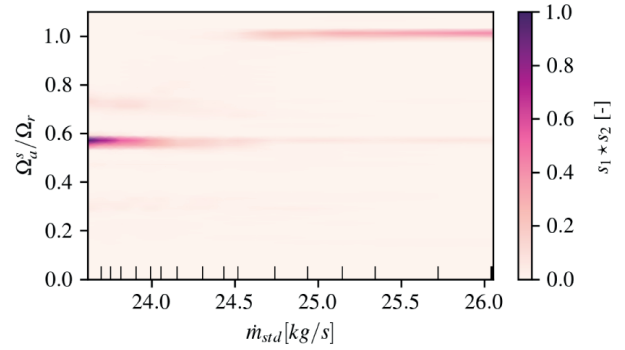


Fig. 11. Transient evolution of group velocity of aerodynamic disturbances during NSV onset at 80% speed, contour of correlation coefficient

These results are a clear validation of the theory on NSV, that convected disturbances have a characteristic propagation speed, in this case 0.56, and can lock-in with the nearest assembly mode of structural vibrations, allowing minor shifts of the propagation speed. In case of ECL5, it is not a single blade and assembly mode that interacts with the aerodynamic disturbances, but multiple, leading to superposed and complex patterns. Mode-2 reaches the highest levels of scope limit, whereas Mode-3 has the most coherent interaction pattern. Mode-1 vibrates at significant amplitude but without a clear nodal

Table 2. Non-Synchronous Vibration modes experimentally observed at 80% speed during NSV (23.6kg/s)

	$\frac{\omega_v^R}{\Omega_r}$ [EO]	N_v [-]	$\frac{\omega_v^S}{\Omega_r}$ [EO]	N_a [-]	$\frac{\omega_a^S}{\Omega_r}$ [EO]	$\frac{\omega_a^R}{\Omega_r}$ [EO]	$\frac{\Omega_a^S}{\Omega_r}$ [-]
Mode-3	5.87	2	7.87	-15	8.44	6.56	0.56
				-14	8.13	5.87	0.58
				-13	7.33	5.67	0.56
				-12	6.77	5.23	0.56
Mode-2	4.52	6	10.52	-10	5.47	4.53	0.55
				-8	4.55	3.45	0.57
				-7	3.98	3.02	0.58
Mode-1	1.87	-5	12.87	5	3.11	1.89	0.63
				4	2.23	1.77	0.56

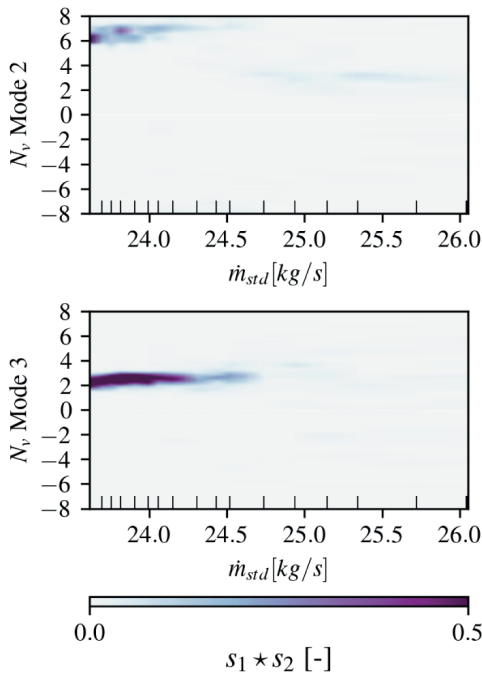


Fig. 12. Transient evolution of the nodal diameter from strain gauge data for Mode-2 and Mode-3 during NSV onset at 80% speed, contour of correlation coefficient

diameter.

Analysis of rotating-stall at design speed

Throttling slowly towards low mass-flow rates at design speed, the machine encounters rotating stall with no vibration precursors. Fig. 13 presents the transient evolution of the static pressure at the casing during 20 revolutions at stall inception. During this maneuver Mode-1 reaches vibration limits of 50% of scope limit, and Mode-2 and Mode-3 respond with levels of approximately 30%. As shown in the figure, a first rotating stall cell arises at the 7th rotation at Blade-13 and propagates around the circumference. Comparable behavior of the rotating stall onset was predicted by URANS simulations presented in paper [27].

COMPARISON WITH NUMERICAL PREDICTION OF NSV

In [22] we show that the prediction of the aerodynamic performance coincides well with the experiment, particularly between respective design conditions and near stall for transonic and subsonic conditions. Exemplarily, Fig. 14 shows the measured total-pressure characteristic at 80% speed compared to a steady RANS simulation. Time-linearized Fluid-Structure Interaction (LRANS/FSI) simulations of the setup predicted stable behaviour of Mode-1 and Mode-3, whereas unstable conditions of nodal diameter $N_v = 5$ were indicated for Mode-2 at a mass-flow rate of 26 kg/s, which was interpreted as flutter according to the used method [28]. Further throttling was

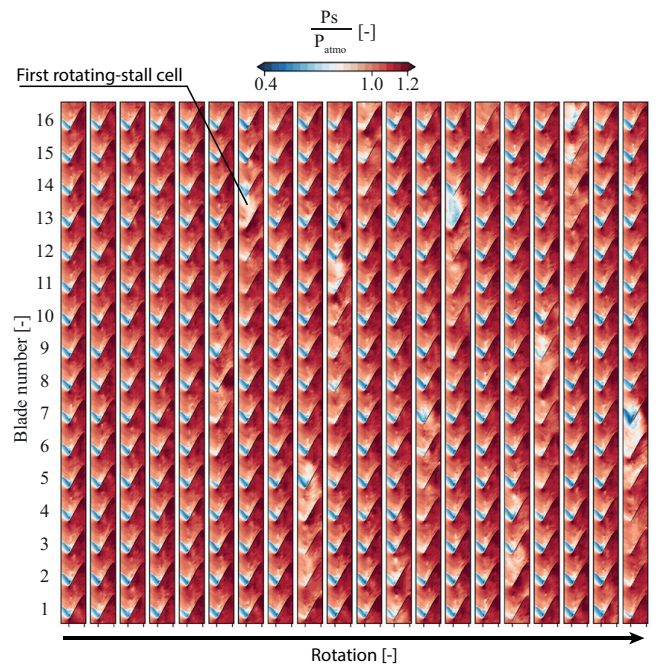


Fig. 13. Transient evolution of static pressure at the casing during the onset of stall at design speed

not possible due to convergence issues. Details on this study are found in [28], which also describes the development process of the fan. In succession of this work, time-accurate URANS/FSI simulations with pre-imposed harmonic blade movement of Mode-2 were carried out and presented at [29]. The full circumference of the spherical air intake and the rotor was meshed with a total number of $34 \cdot 10^6$ nodes with $y^+ \approx 1$. Simulations were performed with elsA [30], an unsteady Reynolds-Averaged Navier-Stokes solver, developed by ONERA. All numerical parameters are detailed in [29]. This study predicted stable conditions for a mass-flow rate of 26 kg/s but could be converged to lower mass-flow of 25 kg/s by using a choked nozzle setup and indicated periodically unstable conditions for nodal diameter $N_v = 4$ at a vibration amplitude of 12.5% scope limit (0.25mm at the tip). Doubling of the vibration amplitude led to stable behaviour at 25% scope limit. For Mode-3 no time-accurate URANS/FSI calculations have been conducted so far, since this mode has been predicted fully stable in previous work. The respective conditions are summarized in Fig. 14. All performed numerical simulations predict the onset of vibration for higher mass-flows than observed in the experiment and mis-predict the critical mode.

In the following, we will briefly assess the discrepancy at the example of the URANS/FSI simulation from [29]. Fig. 15 shows the comparison of unsteady wall pressure measurements with the URANS/FSI simulation of 12.5% scope limit Mode-2/ $N_v=4$. We recall that the vibration amplitude in the experiment is slightly below 10% scope limit for Mode-2 and Mode-3 at 25 kg/s and reaches 50% for Mode-2 at 23.5 kg/s. For orientation, the ensemble averaged wall pressure is shown in the left graphs (a), indi-

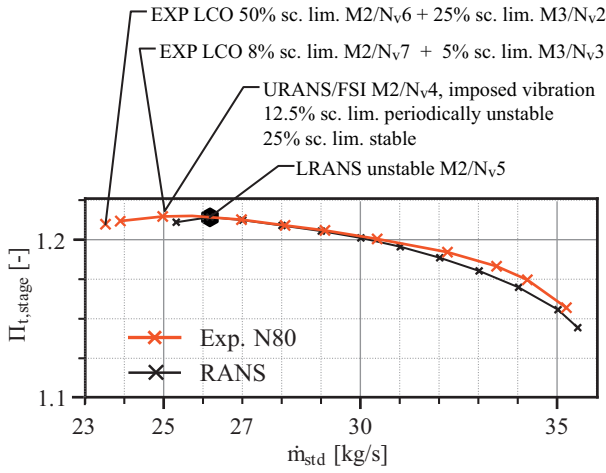


Fig. 14. Predicted instability onset by LRANS/FSI and URANS/FSI compared to experimental stage characteristic at 80% speed

ating excellent prediction of the average flow field by the simulation at 25kg/s. The middle graphs (b) present the unsteady fluctuation of the pressure field during one exemplary revolution. It can be seen, that local aerodynamic disturbances appear in the leading edge plane, such as extensively discussed in [14, 12, 2, 31]. The intensity of these disturbances is significantly stronger in the numerical simulations at 25kg/s mass-flow. In the simulation, a very coherent pattern is observed with strong disturbances observed in multiple channels, while the experiment is much less structured. In the experiment at 23 kg/s the amplitudes of disturbances reach the same level of intensity as the simulation at higher mass-flows and local patterns are comparable with the simulation. The final plots (c) present the temporal standard deviation, hence the average fluctuation of the wall pressure field for each passage. Again, the simulation presents higher average values in the leading edge plane and is obviously symmetric due to the numerical setup with identical blades. In the experiment, the dominant fluctuation zones are observed at similar average position, but the intensity depends on the individual blades. A detailed analysis exceeds the scope of this paper, but indications for correlation with local tip clearance have been observed: for several blades comparably low disturbances are measured in the passage (i.a. 3 and 13), while others show strong fluctuations upstream of the leading edge (i.a. 4 and 14). Regarding the running tip-clearance measurements in [22], the low fluctuation passages correlate with preceding blades of low tip clearance. Additionally, the individual stagger angle is relevant and detailed experimental and numerical studies will be conducted in the future to analyse the dependency.

The main issue for the mis-prediction of the critical nodal diameter of Mode-2 is a deviation of the propagation speed of disturbances. In the numerical simulation, a continuous evolution of propagation speed with massflow rate was reported in [29]. For 26 kg/s mass-flow, the predicted propagation speed was $\Omega_a^s/\Omega_r = 0.55$ and increased to

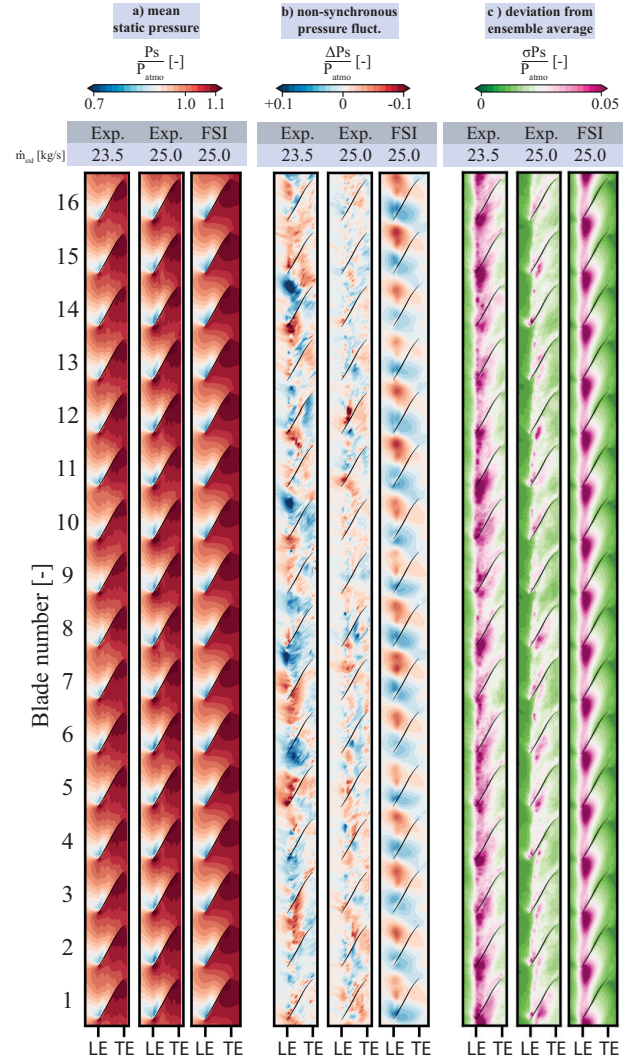


Fig. 15. Blade-to-blade visualizations from experimental data and numerical predictions. Experiment for mass-flow 23.5 kg/s during NSV, and 25.0 kg/s, numerical prediction from URANS/FSI simulation with imposed vibration $M2/N_v4$ (amplitude $\approx 12.5\%$ scope limit) at mass-flow 25.0 kg/s : (a) mean static pressure, (b) non-synchronous pressure fluctuation and (c) deviation from ensemble average

0.63 at mass-flow 25kg/s. The experiments shown in this paper indicate a constant speed of $\Omega_a^s/\Omega_r = 0.56$ for these massflow conditions. The relative deviation is low, but the critical interaction mode is very sensitive.

Using the values of measured blade eigenfrequency and propagation speed for the reduced order model provided by [32, 33] the critical nodal diameter is predicted as in Fig. 16. For 80% speed, the free propagation speed of $\Omega_a^s/\Omega_r = 0.56$ does not coincide with maximum negative damping values of either mode. Instead, lock-in to slightly shifted propagation speeds occurs. The propagation speed predicted by URANS of $\Omega_a^s/\Omega_r = 0.63$ corresponds to a critical nodal diameter of $N_v = 4$. This graph clearly illustrates the necessity of accurate prediction of convective disturbances in simulations and the obvious discrepancy by the employed method. The numerical sim-

ulations predicted a closer value to the experimentally observed disturbance propagation speed for higher mass-flow rates ($\Omega_a^s/\Omega_r = 0.55$ at 26kg/s), but indicated stability in agreement with the measurement.

Hence, the main objective for future work is to improve the prediction accuracy at highly throttled conditions, for example through the adaptation of LES simulations coupled with blade vibration. It has been shown in [34] that full-annulus high fidelity simulations (LES) of the configuration are feasible today, and as the critical modes are known now, the number of necessary simulations is limited. Merely, aeroelastic coupling needs to be employed, either by using harmonic imposed vibration or even using strongly coupled methods.

With the presented dataset and the open geometry, this is a challenge for the whole aeroelastic research community.

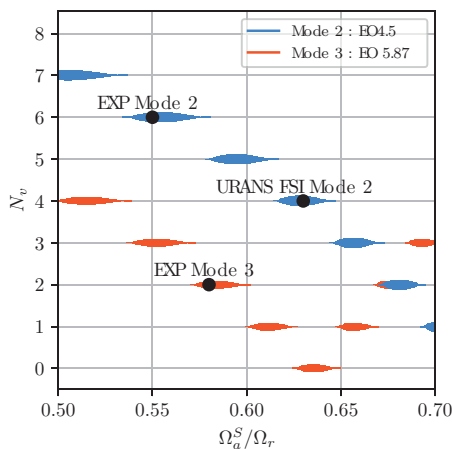


Fig. 16. Result of NSV-Model from [32]: Prediction of critical nodal diameter over aerodynamic propagation speed for Mode-2 and Mode-3. Symbol size proportional to negative aerodynamic damping value.

CONCLUSION

The tuned reference configuration of the open-test-case fan ECL5 has been investigated experimentally using multi-physical instrumentation. The machine has proven fully operational at subsonic and transonic speeds. Synchronous vibration levels of the undistorted machine are low and allow full exploitation of the speed-range up to 105%. With installed instrumentation rakes significant forced response is present and allowed the characterization of structural modes using tip-timing and strain gauge measurements. This study revealed significant differences to ping tests of isolated blades and to FEM predictions, and also quantified the amount of unintended mistuning.

At different speedlines an extensive study of the stability limit has been conducted and presented. At transonic speeds, rotating stall was observed without vibratory

precursors. In the whole subsonic regime between 55% and 90% of design speed significant non-synchronous vibrations of different eigenmodes were observed, reaching scope limits of up to 50% for the second blade eigenmode. All total-pressure characteristics are rolled over and limit-cycle vibration levels continuously rise with decreasing mass-flow.

A detailed analysis of the aeroelastic coupling at 80% speed was presented and allowed a clear identification of convected disturbances, which lock-in with the second and third eigenmode. Furthermore a multitude of non locked-in aerodynamic disturbances could be identified. Interaction with trapped acoustic modes was not observed and neither a classical flutter mechanism.

Comparison with already published FSI simulations of the setup has revealed the challenge to accurately predict the instability behaviour of this novel generation of fans. Even though the average flow field was predicted with high accuracy, a slight mis-prediction of convective propagation speed caused the wrong nodal diameter to become critical. Furthermore, the machine simultaneously developed vibration patterns in multiple eigenmodes, specifically for a mode that was predicted to be completely stable in simulations.

The presented dataset is considered a benchmark for future aeroelastic method development. The full geometry details, structural properties and modal deformations are shared with the community as will be raw data of the measurements within the next year. The authors encourage researchers to apply for the test-case geometry. Results presented here and in the accompanying paper on the aerodynamic investigation provide all relevant conditions to validate numerical simulations on different levels of fidelity.

ACKNOWLEDGMENTS

The results presented in this paper rely on the contributions of a large research group and the authors gratefully acknowledge the excellent collaboration and support over the past five years. The authors particularly thank Pavel Teboul, Cedric Desbois, Sebastien Goguy, Gilbert Halter, Lionel Pierrard, Laurent Pouilloux, Edouard Salze of LMFA, Kevin Billon and Claude Gibert of LTDS for their support and contributions to the experiments.

The authors recall that the development of the fan was conducted within the thesis of Valdo Pages and supervised by Stephane Aubert, Pascal Ferrand, Pierre Duquesne from LMFA and Laurent Blanc from LTDS. The final design was developed in close collaboration with Safran Aircraft Engines, and the authors particularly acknowledge the help of Laurent Jablonski. We are grateful for the continuous collaboration and financial support of SAFRAN Aircraft Engines since the beginning of this project and specifically for the present measurement campaign, for which the test module MARLYSA was provided by SAFRAN.

For the tip-timing measurements we received exten-

sive support of Gerhard Ziller, Marco Hermann and Simon Kytzia of MTU Aero Engines.

The presented research was financed through the European Union's Clean Sky 2 Joint Undertaking (JU) under grant agreement N864719, CATANA. The JU receives support from the European Union's Horizon 2020 research and innovation program and the Clean Sky 2 JU members other than the Union. The paper reflects only the author's view and the JU is not responsible for any use that may be made of the information it contains. Assessment of the test facility was enabled through financial supports of Agence Nationale de la Recherche (ANR, Project d'EquipEx PHARE) and Conseil pour la Recherche Aeronautique Civile (CORAC - Programme CUMIN). Buildings and infrastructure were supported by ECL, instrumentation supported by Institut Carnot (INGENIERIE@LYON - Project MERIT) and SAFRAN Aircraft Engines.

REFERENCES

- [1] Mailach, R., Lehmann, I., and Vogeler, K., 2001. "Rotating instabilities in an axial compressor originating from the fluctuating blade tip vortex". *J. Turbomach.*, **123**(3), pp. 453–460.
- [2] Pullan, G., Young, A., Day, I., Greitzer, E., and Spakovszky, Z., 2015. "Origins and structure of spike-type rotating stall". *J. Turbomach.*, **137**(5), pp. 51007–51011.
- [3] Baumgartner, M., Kameier, F., and Hourmouziadis, J., 1995. "Non-engine order blade vibration in a high pressure compressor". In Proc. 12th ISABE (International Society for Air Breathing Engines).
- [4] Mailach, R., Sauer, H., and Vogeler, K., 2001. "The periodical interaction of the tip clearance flow in the blade rows of axial compressors". In Proc. ASME Turbo Expo 2001.
- [5] Rendu, Q., Stapelfeldt, S., Salles, L., and Vahdati, M., 2019. "Identification of low speed fan flutter trigger through radial decomposition of the modeshape". In International Gas Turbine Congress.
- [6] Kersken, H.-P., Ashcroft, G., Frey, C., Wolfrum, N., and Ptz, O., 2018. "Comparison of Linear and Nonlinear Frequency Domain Methods for Flutter Analysis". Vol. Volume 2C: Turbomachinery of *Turbo Expo: Power for Land, Sea, and Air*.
- [7] Schuff, M., and Chenaux, V. A., 2020. "Coupled Mode Flutter Analysis of Turbomachinery Blades Using an Adaptation of the P-K Method". Vol. Volume 10A: Structures and Dynamics of *Turbo Expo: Power for Land, Sea, and Air*.
- [8] Beselt, C., Pardowitz, B., Rennings, R., Sorge, R., Peitsch, D., Enghardt, L., Thiele, F., Ehrenfried, K., and Thamsen, P., 2013. "Influence of the clearance size on rotating instability in an axial compressor stator".
- [9] Schoenenborn, H., Junge, M., and Retze, U., 2012. "Contribution to Free and Forced Vibration Analysis of an Intentionally Mistuned Blisk". Vol. Volume 7: Structures and Dynamics, Parts A and B of *Turbo Expo: Power for Land, Sea, and Air*, pp. 1111–1120.
- [10] Yumer, M. E., Cigeroglu, E., and Ozguven, H. N., 2013. "Mistuning Identification of Integrally Bladed Disks With Cascaded Optimization and Neural Networks". *Journal of Turbomachinery*, **135**(3), 03.
- [11] Eggers, T., Friedrichs, J., Goessling, J., Seume, J. R., Natale, N., Fih, J. P., and Paletta, N., 2021. "Composite UHBR Fan for Forced Response and Flutter Investigations". Vol. Volume 2A: Turbomachinery Axial Flow Fan and Compressor Aerodynamics of *Turbo Expo: Power for Land, Sea, and Air*.
- [12] Kielb, R., Barter, J., Thomas, J., and Hall, K., 2003. "Blade excitation by aerodynamic instabilities: A compressor blade study". In Proc. ASME Turbo Expo 2003, pp. 399–406.
- [13] Rodrigues, M., Soulat, L., Paoletti, B., Ottavy, X., and Brandstetter, C., 2021. "Aerodynamic investigation of a composite low-speed fan for uhbr application". *J. Turbomach.*, **143**(10), p. 101004.
- [14] Brandstetter, C., Juengst, M., and Schiffer, H.-P., 2018. "Measurements of radial vortices, spill forward, and vortex breakdown in a transonic compressor". *J. Turbomach.*, **140**(6), p. 061004.
- [15] Vahdati, M., and Cumpsty, N., 2016. "Aeroelastic instability in transonic fans". *J. Eng. Gas Turbines and Power*, **138**(2), p. 22604.
- [16] Berthold, C., Krack, M., and Frey, C., 2022. "Fully coupled analysis of flutter induced limit cycles: Frequency vs. time domain methods".
- [17] Peters, A., Spakovszky, Z. S., Lord, W. K., and Rose, B., 2014. "Ultra-short Nacelles for Low Fan Pressure Ratio Propulsors". *Journal of Turbomachinery*, **137**(2), 09.
- [18] Wilson, M. J., Imregun, M., and Sayma, A. I., 2006. "The effect of stagger variability in gas turbine fan assemblies". *J. Turbomach.*, **129**(2), pp. 404–411.
- [19] Lu, Y., Green, J., Stapelfeldt, S., and Vahdati, M., 2019. "Effect of geometric variability on running shape and performance of a transonic fan". *J. Turbomach.*, p. 101012.
- [20] Pages, V., Duquesne, P., Aubert, S., Blanc, L., Ferrand, P., Ottavy, X., and Brandstetter, C., 2022. "Uhbr open-test-case fan ecl5/catana". *International Journal of Turbomachinery, Propulsion and Power*, **7**(2).
- [21] Brandstetter, C., Pages, V., Duquesne, P., Paoletti, B., Aubert, S., and Ottavy, X., 2019. "Project phare-2 : A high-speed uhbr fan test facility for a new open-test case". *J. Turbomach.*, **141**(10), p. 101004.
- [22] Schneider, A. P., Fiquet, A.-L., Paoletti, B., Ottavy, X., and Brandstetter, C., 2023. "UHBR Open-Test-Case Fan ECL5/CATANA: The experimental reference". In To be published GT2023-103629.
- [23] Pages, V., Duquesne, P., Ottavy, X., Ferrand, P., Aubert, S., Blanc, L., and Brandstetter, C., 2021. "Uhbr open-test-case fan ecl5/catana, part 2 : Mechanical and aeroelastic stability analysis". In Proc. 14th European Conference on Turbomachinery Fluid dynamics and Thermodynamics, ETC2021-625.
- [24] Schneider, A. P., Paoletti, B., Ottavy, X., and Brandstetter, C., 2022. "Influence of a turbulence control screen on the aerodynamic and aeroelastic behavior of a UHBR fan".
- [25] Zielinski, M., and Ziller, G., 2000. "Noncontact vibration measurements on compressor rotor blades". *Measurement Science and Technology*, **11**, pp. 847 – 856.
- [26] Brandstetter, C., Ottavy, X., Paoletti, B., and Stapelfeldt, S., 2021. "Interpretation of stall precursor signatures". *J. Turbomach.*, **143**(12), p. 121011.
- [27] Fiquet, A.-L., Ottavy, X., and Brandstetter, C., 2022. "UHBR Open-Test-Case Fan ECL5/CATANA: Numerical Investigation Near the Stability Limit Including Aerodynamic Mistuning". In Proc. ASME. GT2022, Volume 6B: Turbomachinery, GT2022-77992, p. V06BT15A001.
- [28] Pages, V., 2021. "Conception du fan uhbr ecl5 pour une analyse des mécanismes d'interactions multi-physiques à l'origine du flottement". PhD thesis. Thèse de doctorat dirigée par Aubert, Stephane Mécanique des fluides et énergétique Lyon 2021.
- [29] Fiquet, A.-L., Ottavy, X., and Brandstetter, C., 2022. "UHBR Open-Test-Case Fan ECL5/CATANA: Non-linear analysis of non-synchronous blade vibration at part-speed conditions". In 16th International Symposium on Unsteady Aerodynamics, Aeroacoustics and Aeroelasticity of Turbomachines, Toledo, Spain, Sept.
- [30] Cambier, L., Heib, S., and Plot, S., 2013. "The onera elsA cfd software: input from research and feedback from industry". *Mechanics and Industry*, **14**(3), pp. 159–174.
- [31] Young, A., Day, I., and Pullan, G., 2012. "Stall warning by blade pressure signature analysis". *J. Turbomach.*, **135**(1), p. 11033.
- [32] Stapelfeldt, S., and Brandstetter, C., 2020. "Non-synchronous vibration in axial compressors: Lock-in mechanism and semi-analytical model". *J. Sound and Vibration*, **488**, p. 115649.
- [33] Brandstetter, C., and Stapelfeldt, S., 2021. "Analysis of a linear model for non-synchronous vibrations near stall". *Int. J. Turbo-mach., Propulsion and Power*, **6**(3), p. 26.
- [34] Al-Am, J., Clair, V., Giauque, A., and Boudet, J., 2021. "A Parametric Study on the LES Numerical Setup to Investigate Fan/OGV Broadband Noise". *International Journal of Turbomachinery, Propulsion and Power*, **6**(2), p. 12.



The presented research was supported through Clean Sky 2 Joint Undertaking (JU), project CATANA under grant agreement N°864719. The JU receives support from the European Union's Horizon 2020 research and innovation programme and the Clean Sky 2 JU members other than the Union. This publication reflects only the author's view and the JU is not responsible for any use that may be made of the information it contains.

catana.ec-lyon.fr

Christoph.brandstetter@ec-lyon.fr

